



PAPER

Single layer vanadium oxide assisted switchable metasurfaces for transmissive and reflective polarization conversion

RECEIVED
8 August 2024REVISED
3 October 2024ACCEPTED FOR PUBLICATION
10 October 2024PUBLISHED
21 October 2024Thi Quynh Hoa Nguyen* , Thi Minh Nguyen and Hong Quang Nguyen

School of Engineering and Technology, Vinh University, 182 Le Duan, Vinh, 460000, Vietnam

* Author to whom any correspondence should be addressed.

E-mail: ntqhoa@vinhuni.edu.vn

Keywords: switchable metasurface, reflection, transmission, polarization conversion

Abstract

Polarization control using metasurfaces is highly advantageous; however, most metasurfaces operate exclusively in either transmission or reflection mode. Additionally, achieving both wide bandwidth and high efficiency simultaneously in their design remains a significant challenge. Here, we design a high-efficiency and wideband switchable metasurface that can switch between transmissive and reflective polarization conversion modes by utilizing a single layer of I-shaped resonators and gold-vanadium dioxide (VO₂) alternating gratings printed on a quartz substrate. When VO₂ transitions to its metallic phase, the continuous metal layers of gold-VO₂ eliminate transmission and the designed metasurface operates as a reflective cross-polarization converter with a polarization conversion ratio (PCR) exceeding 0.9 over a broad frequency range of 1.4–3.3 THz. Conversely, when VO₂ is in its insulator phase, the THz incoming wave can transmit through the gratings, and the design behaves as a transmissive cross-polarization converter with a PCR above 0.99 in the 0.75–4.0 THz range for a forward *y*-polarized wave. The working mechanism for both transmissive and reflective polarization conversion modes is explained through theoretical analysis and surface current distributions. With the advantages of facile design, high performance, and dual functionality, our design is expected to be applied in the fields of imaging, sensing, and communication.

1. Introduction

Controlling electromagnetic (EM) waves is fundamental to light–matter interactions and has numerous applications, such as polarization imaging [1–3], optical data storage [4, 5], and information multiplexing [6–8]. Traditional methods for manipulating EM wave polarization, such as the optical activity of crystals or the Faraday effect, are often unsuitable for many practical applications due to limitations like bulky volume, sensitivity to incidence angle, and narrow relative bandwidth [9].

Metasurfaces are engineered two-dimensional structures, offer the capability to arbitrarily manipulate light using extremely thin components. They can simply replace bulky optical systems, but in addition, they are capable of providing new functionalities that are not achievable with traditional components. However, most polarization control-based metasurfaces can be designed to operate in either transmission [10–16] or reflection modes [9, 17–21]. To address this issue, the integration of metasurfaces with phase change materials (PCMs) has been proposed to realize diversified functionalities [22–36]. Among PCMs, vanadium dioxide (VO₂) exhibits a fast response, large modulation depth, and multiple modulation methods [37], as well as a low phase change temperature of 68°C [38]; therefore, it is widely used for THz multifunctional metasurfaces. Based on this approach, metasurface structures capable of achieving polarization conversion functions in both reflection and transmission modes have been developed. For example, Jiang *et al* [39] presented a metamaterial configuration to achieve both reflective and transmissive cross-polarization converters by utilizing the phase transition characteristics of VO₂, which yielded a reflective polarization conversion (RPC) from 4.8 to 13.13 THz and a transmissive polarization conversion (TPC) from 0.5 to 4.75 THz. Similarly, Wang *et al* [40] proposed a tunable

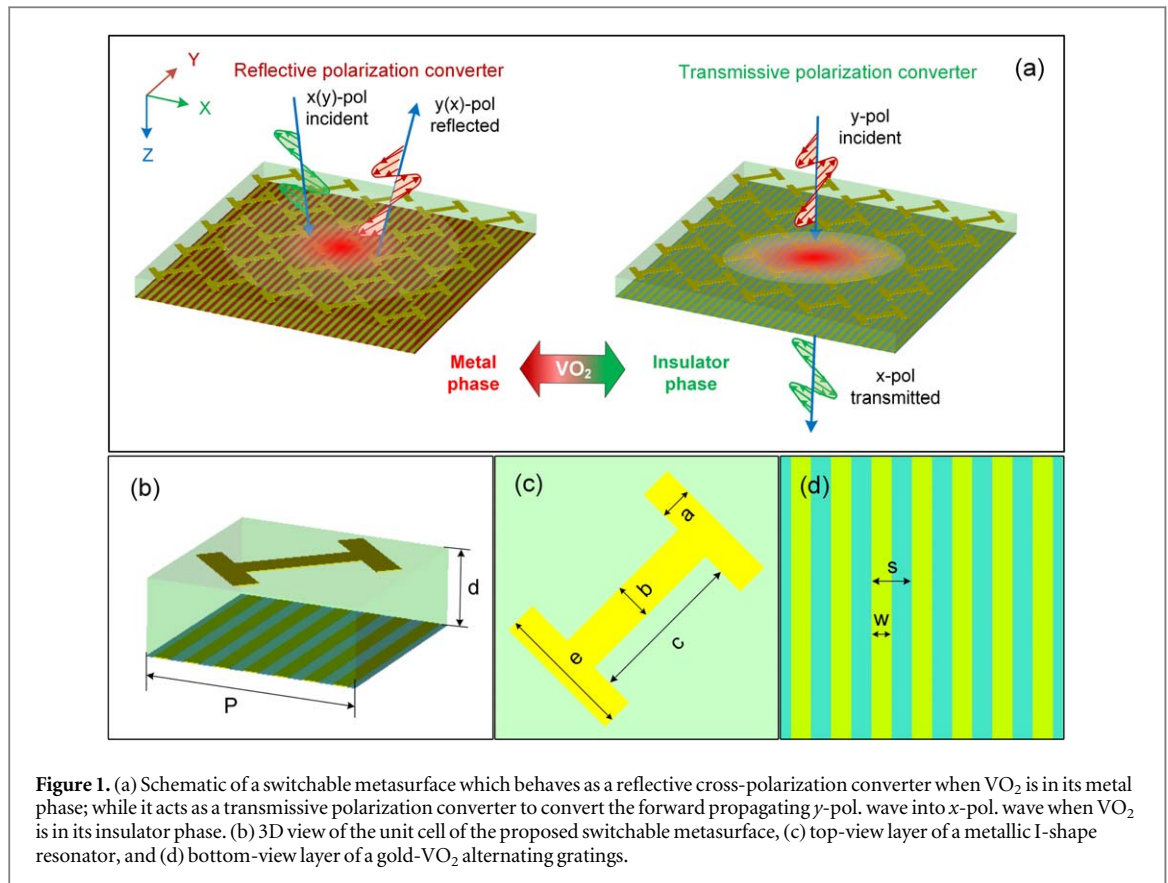


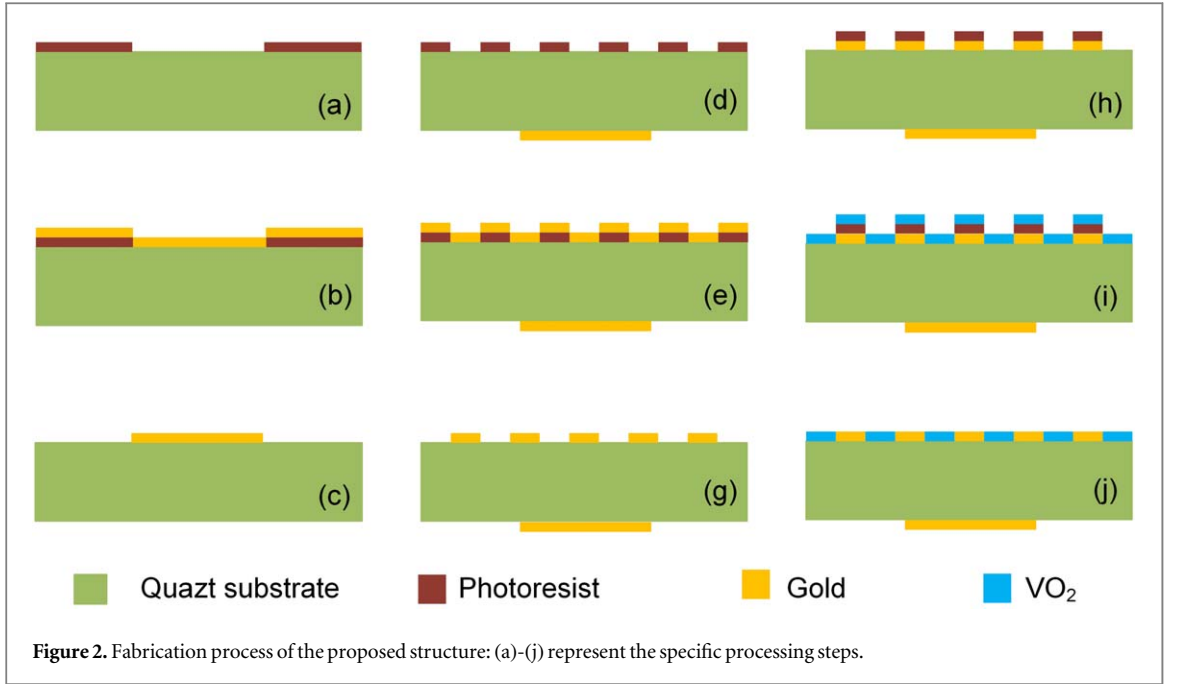
Figure 1. (a) Schematic of a switchable metasurface which behaves as a reflective cross-polarization converter when VO_2 is in its metal phase; while it acts as a transmissive polarization converter to convert the forward propagating y -pol. wave into x -pol. wave when VO_2 is in its insulator phase. (b) 3D view of the unit cell of the proposed switchable metasurface, (c) top-view layer of a metallic I-shape resonator, and (d) bottom-view layer of a gold- VO_2 alternating gratings.

wide-angle chiral metamaterial incorporating VO_2 , which can realize different operating modes and polarization conversions in the THz region. Despite their wide operating bandwidth, the use of cascaded dielectric substrates and metallic gratings makes these structures complex, resulting in challenges with fabrication and higher costs. More recently, another approach based on embedding PIN diodes into the metasurface structure has been explored to dynamically control wideband TPC and RPC responses [41, 42]. However, this approach suffers from low efficiency, narrow bandwidth, and structural complexity, and is suitable only for the microwave region. Hence, the development of a simple tunable metasurface capable of achieving high-performance polarization conversion in both transmission and reflection modes simultaneously remains a challenge.

In this paper, we propose a simple design for a high-efficiency and wideband switchable metasurface that can switch between TPC and RPC modes by utilizing a single layer of quartz substrate with gold I-shaped resonators and gold- VO_2 alternating gratings printed on both sides. In this design, the gold- VO_2 alternating gratings layer acts as the switching layer, enabling the structure to switch between transmission and reflection modes by changing the phase of VO_2 from an insulator to a metal. Once VO_2 is in its insulator phase, the metasurface can realize wideband TPC with high conversion efficiency of over 0.99 from 0.75 to 4.0 THz. Conversely, when VO_2 is in its fully metal phase, it can exhibit RPC with its efficiency exceed 0.9 in a broad frequency range of 1.4-3.3 THz for LP waves. This design highlights significant potential for a range of THz applications, including imaging, sensing, and communication.

2. Structural model and method

The schematic of the switchable metasurface (SM) between RPC and TPC modes for linearly polarized (LP) waves is illustrated in figure 1. By altering the conductivity of VO_2 through phase changes from metallic to insulator via thermal treatment, the proposed SM can switch its functions from RPC to TPC, as demonstrated in figure 1(a). The proposed SM structure consists of a metal/insulator/metal (MIM) configuration. The bottom metallic layer of a gold- VO_2 alternating gratings plays as switchable function layer (figure 1 (c)). When VO_2 is in its metallic phase, this layer behaves a fully metallic layer and the proposed SM structure with a metal I-shaped resonator layer and the fully metallic layer sandwiched by a dielectric layer acts as a RPC due to the diagonal symmetry of I-shaped resonator (figure 1 (b)). Meanwhile, when VO_2 stays in an insulator phase, the proposed SM structure with a diagonal symmetry resonator layer and a metal gratings layer separated by a dielectric layer



plays acts as TPC. It is important to emphasize that the novelty of the proposed metasurface lies in its ability to actively switch between reflection and transmission modes, marking a significant advancement over traditional polarization converters, which typically operate in either reflection or transmission mode.

In this design, the dielectric layer is made of quartz substrate, which has a dielectric constant of 3.75, a loss tangent of 0.0004, and a thickness of $d = 15 \mu\text{m}$. The metal layers is made of gold (Au) with electrical conductivity of $4.56 \times 10^7 \text{ S/m}$ and the thickness of $0.2 \mu\text{m}$. The frequency-dependent permittivity of the VO_2 material is determined using the Debye formula [27, 32, 43]:

$$\epsilon(\omega) = \epsilon_\infty - \epsilon_p^2(\sigma)/(\epsilon^2 + i\gamma\epsilon) \quad (1)$$

with epsilon infinity $\epsilon_\infty = 12$ and the collision frequency $\gamma = 5.75 \times 10^{13} \text{ rad/s}$ [32]. The plasma frequency is calculated by:

$$\epsilon_p^2(\sigma) = (\sigma/\sigma_0)\epsilon_p^2(\sigma_0) \quad (2)$$

where $\sigma_0 = 3 \times 10^5 \text{ S m}^{-1}$ and $\epsilon_p^2(\sigma_0) = 1.4 \times 10^{15} \text{ rad/s}$. VO_2 is a phase transition material that changes from an insulator to a metal when the temperature exceeds 68°C [38]. The conductivity σ of VO_2 is 200 S/m in the insulator phase and $2 \times 10^5 \text{ S/m}$ in the metal phase [38].

The commercial software CST Microwave Studio is used to simulate the model and optimize the structure. In this simulation setup, the unit cell is aligned with the x - and y -axes, and an open boundary condition is applied along the z -axis. Based on the CST simulation, the optimized parameters for the structure are obtained as follows: $P = 42 \mu\text{m}$, $a = 5 \mu\text{m}$, $b = 5.6 \text{ mm}$, $c = 23 \mu\text{m}$, $e = 20 \mu\text{m}$, $w = 3 \mu\text{m}$, and $s = 6 \mu\text{m}$. The proposed metasurface has unit cell dimensions of $42 \mu\text{m} \times 42 \mu\text{m} \times 15 \mu\text{m}$, compatible with current fabrication techniques. The micro-scale structure can be patterned using conventional photolithography on quartz substrates. Thin films of VO_2 and gold can be deposited using pulsed laser deposition (PLD) and sputtering methods, respectively. Additionally, THz Time-Domain Spectroscopy (THz-TDS) can be employed to measure the transmission and reflection spectra of the metasurface in the THz range. The feasibility of fabricating our design is demonstrated in figure 2. The fabrication process begins with a double-side-polished quartz wafer: (a) photoresist is spin-coated, followed by optical lithography; (b) a 200-nm-thick Au layer is deposited on the quartz substrate via sputtering; (c) the photoresist is removed by a lift-off process to form the Au I-shaped resonator; (d) photoresist is spin-coated again and optical lithography is performed to pattern the gold gratings; (e) a 200-nm-thick Au layer is deposited using sputtering; (f) the photoresist is dissolved via lift-off to form the Au gratings; (g) photoresist is spin-coated once more and optical lithography is conducted; (h) a 200-nm-thick VO_2 layer is deposited using the PLD method; (i) the photoresist is dissolved by lift-off, forming alternating Au- VO_2 gratings, and the remaining VO_2 is annealed at 450°C [24].

The relationship between incident and transmitted electromagnetic waves is characterized by the Jones matrix (T), as described by [44].

$$\begin{pmatrix} E_x^{tr} \\ E_y^{tr} \end{pmatrix} = \begin{bmatrix} t_{xx}^{f(b)} & t_{xy}^{f(b)} \\ t_{yx}^{f(b)} & t_{yy}^{f(b)} \end{bmatrix} \begin{pmatrix} E_x^{in} \\ E_y^{in} \end{pmatrix} = T_{lin}^{f(b)} \begin{pmatrix} E_x^{in} \\ E_y^{in} \end{pmatrix} \quad (3)$$

where, the superscripts f and b indicate the propagation of electromagnetic waves in the forward ($+z$) and backward ($-z$) directions, respectively. The subscripts x and y denote the polarization directions of the electromagnetic waves.

To assess the performance of linear polarization conversion for both TPC and RPC modes, the polarization conversion ratio (PCR) is used. The PCR for TPC mode is defined by the following equations [14]:

$$PCR_x = \frac{|t_{yx}|^2}{|t_{yx}|^2 + |t_{xx}|^2} \quad (4)$$

$$PCR_y = \frac{|t_{xy}|^2}{|t_{xy}|^2 + |t_{yy}|^2} \quad (5)$$

$$T_{ij} = |t_{ij}| \quad (6)$$

where t_{ij} denotes the transmission coefficient of the wave polarized in the i direction, resulting from an incident wave polarized in the j direction ($i, j = x$ or y). Meanwhile, the PCR for RPC mode is determined by following equations [19, 21]:

$$PCR_x = \frac{|r_{yx}|^2}{|r_{yx}|^2 + |r_{xx}|^2} \quad (7)$$

$$PCR_y = \frac{|r_{xy}|^2}{|r_{xy}|^2 + |r_{yy}|^2} \quad (8)$$

where, r_{xx} and r_{yy} are the reflection coefficients of the co-polarization waves and r_{xy} and r_{yx} are the reflection coefficients of the cross-polarization waves.

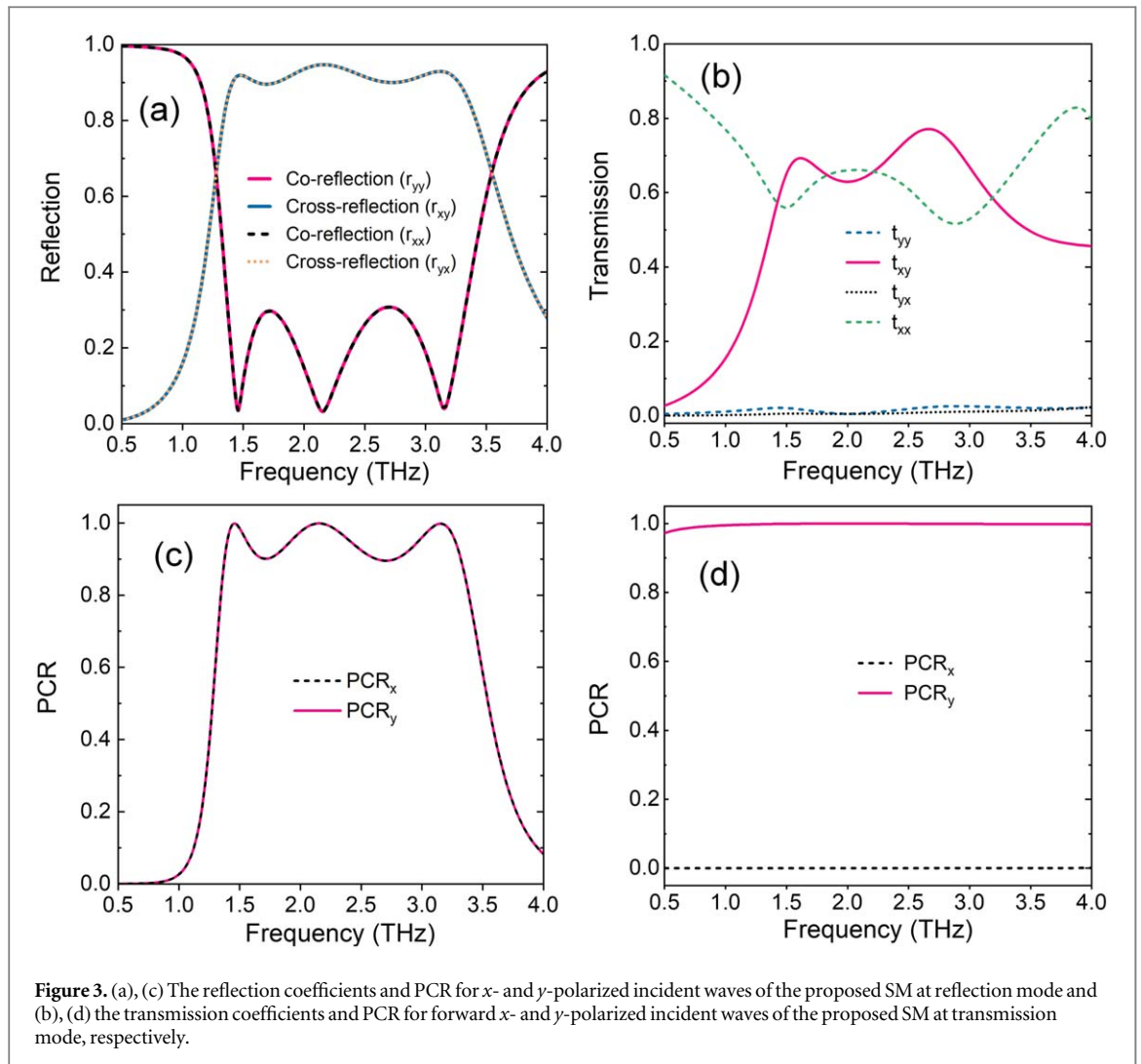
3. Results and discussion

3.1. Switching between transmission and reflection polarization conversion modes

The switchable functionalities from RPC mode to TPC mode of the proposed metasurface can be achieved by thermal treatment to change the conductivity of the VO₂ material. At room temperature, VO₂ remains in an insulator state with a low conductivity of 200 S/m [38]. Thus, the incoming THz wave interacts with a metal-insulator-metal (MIM) configuration of a gold I-shaped resonator layer/insulator layer/gold gratings layer and propagates through the bottom metal gratings layer, allowing the proposed metasurface to operate in TPC mode. In contrast, when the temperature is increased above the phase-change temperature of 68°C [38], VO₂ transitions to a fully metallic state with a high conductivity of 2×10^5 S/m [38]. Therefore, the bottom gold-VO₂ alternating gratings layer becomes a continuous metallic layer that can eliminate transmission. As a result, this MIM configuration can operate in RPC mode.

The switchable functionalities from RPC mode to LPC mode of the proposed metasurface can be obtained by controlling the VO₂ state from metallic to insulator phases. To evaluate the operating modes of the proposed SM, we simulate the conductivity change of VO₂ material from metallic to insulator phases to obtain the reflection and transmission coefficients for both x - and y -polarized incident waves, respectively, as shown in figure 3. As shown in figure 3(a), when VO₂ is in its metallic state, the amplitude of the cross-polarization coefficients (r_{xy} and r_{yx}) of above 0.9 is significantly higher than that of the co-polarization coefficients (r_{xx} and r_{yy}) of below 0.25 in the frequency range from 1.4 THz to 3.3 THz. It is demonstrated that the majority of the incident x -/ y -polarized waves are converted into reflected y -/ x -polarized waves. Due to the symmetrical structure, the spectra of PCR _{x} and PCR _{y} for x - and y -polarized incident waves are equal and their PCR values are greater 0.9 in the wide frequency range of 1.4-3.3 THz, as depicted in figure 3(c). Furthermore, there are three resonant peaks with PCR values close to 1, observed at frequencies of 1.45 THz, 2.16 THz, and 3.16 THz. It indicates that the proposed SM operates efficiently as a linear and wideband reflection polarization converter.

Meanwhile, once VO₂ is in the insulator phase, transmission coefficients of LP waves passing through the proposed metasurface along the forward ($+z$) direction is simulated and depicted in figure 3(b). For forward y -polarized incident waves, the magnitude of cross-polarization transmission t_{xy} is much higher than that of the co-transmission coefficient t_{yy} . Furthermore, t_{xy} for forward ($+z$) incident waves exists two resonant peaks and reaches maximum of 0.65 and 0.78 at the frequencies of 1.6 and 2.6 THz, respectively. In the investigated frequency range of 0.5-4.0 THz, the remarkable difference between t_{xy} and t_{yy} indicates that most of the incident y -polarized wave is transformed into the x -polarized wave for forward ($+z$) incident wave. Conversely, the cross-polarized transmission coefficient (t_{yx}) is nearly zero for forward x -polarized incident waves. Therefore, the



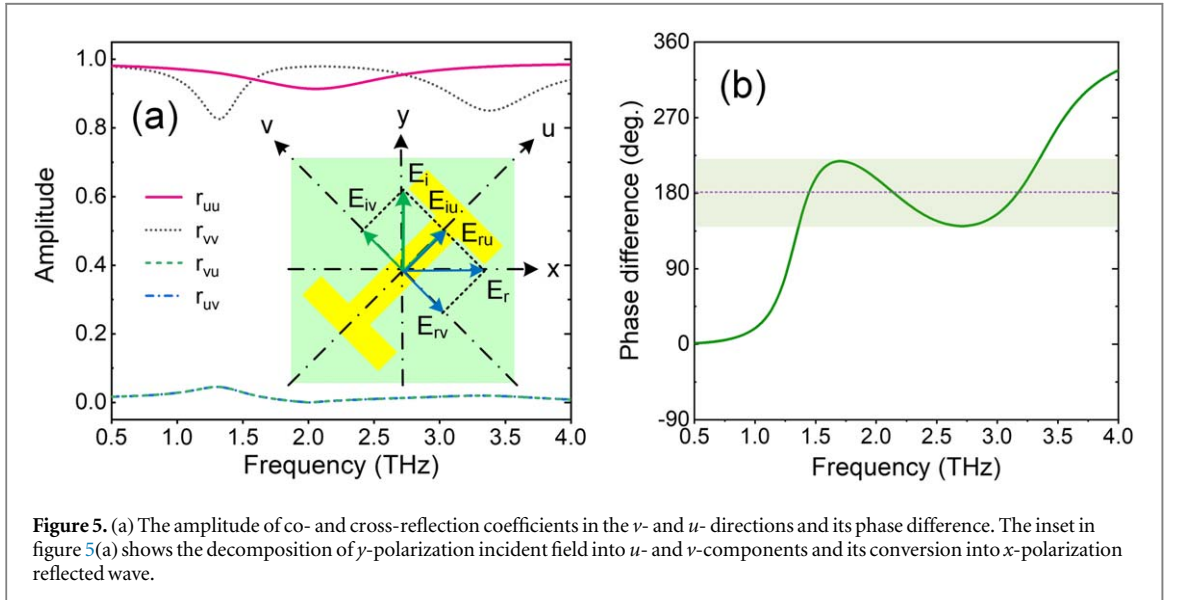
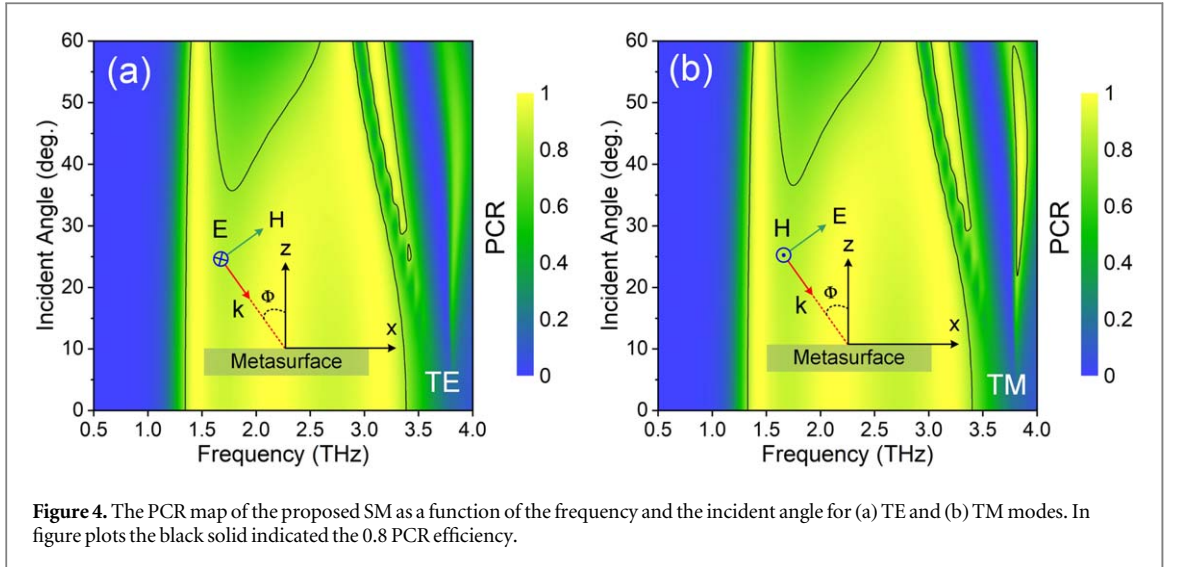
incident x -polarized wave cannot be orthogonally transformed into a y -polarized wave for forward ($+z$) incident waves. This is due to the bottom metal gratings being placed parallel to the y -axis. The calculated PCR for the TPC mode is demonstrated in figure 3(d). It shows that PCR_y exceeds 99% in the frequency range from 0.75 to 4.0 THz, whereas PCR_x is nearly zero within this range. It is evident that the proposed metasurface can effectively work as a cross-polarization converter for forward y -polarized incident waves in transmission mode. The calculated relative bandwidth (RBW), defined as $\text{RBW} = 2(f_H - f_L)/(f_H + f_L)$, where f_H and f_L are the upper and lower frequencies with efficiency above 0.99 and 0.9 for TPC and RPC modes, respectively, reaches about 136.8% and 80.8%, indicating a good wideband polarization conversion property in both transmission and reflection modes.

3.2. Analysis of reflection polarization conversion

In real-world applications, electromagnetic waves typically arrive from various angles. Angular stability ensures that the metasurface maintains optimal performance, such as polarization conversion efficiency, even at non-normal incidence. Therefore, the angular stability of metasurface structures is essential for practical applications in communications, radar, and optics. The influence of the incident angle on PCR for both TE and TM modes is investigated and shown in figures 4(a) and (b), respectively. The simulated results are gathered for y -polarized incident waves.

As the incident angle increases from 0 – 35° , the PCR efficiency can maintain as high as 0.8 while the bandwidth tends to narrow slightly in the high frequency band for both TE and TM modes. This demonstrates that the SM structure exhibits wide-angle stability for the RPC feature in both TE and TM polarization modes. It was reported that the shrinkage of bandwidth of the metasurface with increasing the incident angle is due to the destructive interference at the surface of the designed structure at large incident angles [17, 19].

To investigate the polarization conversion performance of the proposed structure, a theoretical analysis is conducted. In the inset of figure 5(a) illustrates the working principle of the proposed SM structure. Assuming that incident EM wave (E_i) is along to the y -axis and decomposes into u - and v -components. The u - and v -axes are rotated $\pm 45^\circ$ relative to the y -axis, as shown in the inset of figure 5(a). The incident wave (E_i) and reflected



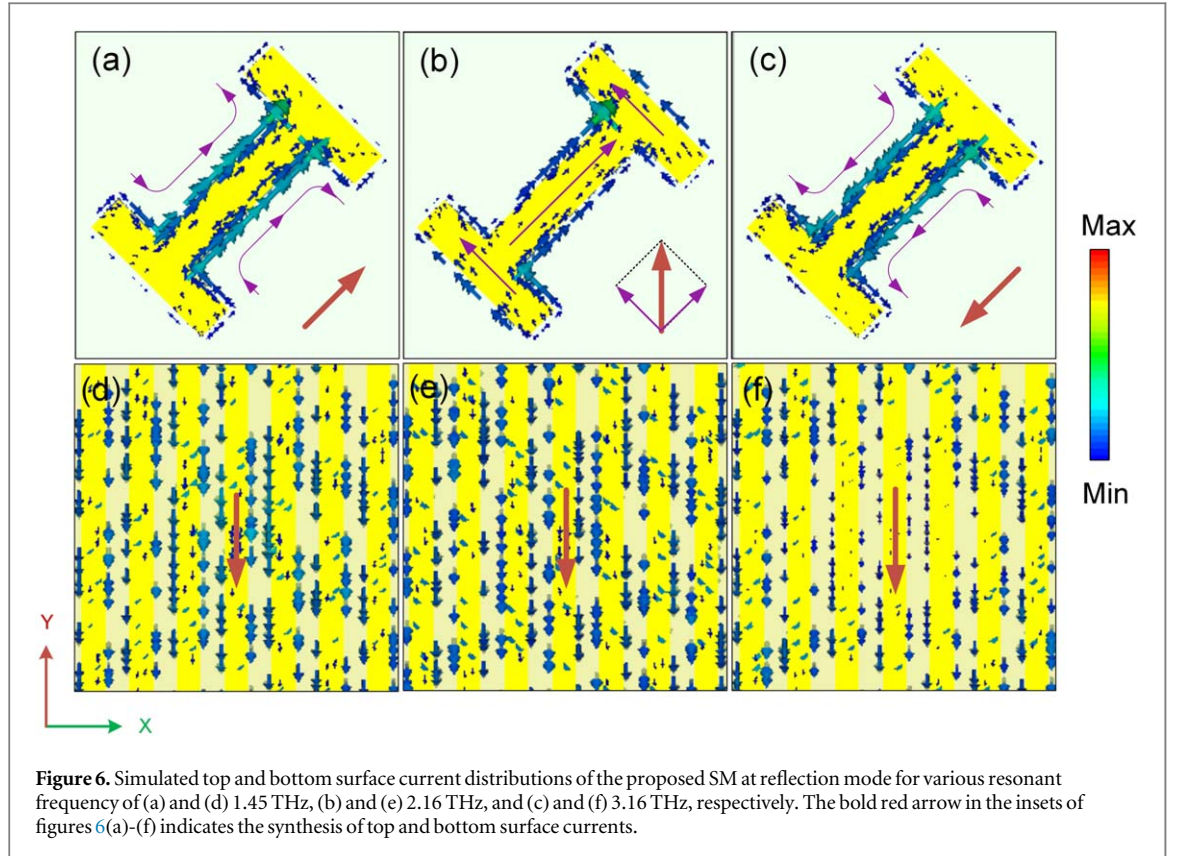
wave (E_r) are described by equations (9) and (10), respectively.

$$E_i = \hat{y}E_i = \hat{u}E_i + \hat{v}E_i \quad (9)$$

$$E_r = \hat{x}r_{xy}E_i = \hat{u}r_{uu}E_{iu}e^{i\Phi_{uu}} + \hat{v}r_{vv}E_{iv}e^{i\Phi_{vv}} \quad (10)$$

where, \hat{x} , \hat{y} , \hat{u} , \hat{v} are the unit vector, r_{uu} , r_{vv} and Φ_{uu} , Φ_{vv} are the magnitude and phase of u - and v -components of the co-polarization reflection coefficients, respectively. If $r_{uu} = r_{vv} \approx 1$, $r_{uv} = r_{vu} \approx 0$, and the phase difference $\Delta\varphi = |\Phi_{uu} - \Phi_{vv}| = 180^\circ + 2k\pi$, the synthetic fields E_{ru} and E_{rv} will be aligned with the x -axis, as demonstrated in figure 5(a). Figures 5(a) and (b) shows the magnitude of reflection coefficients of u - and v -components at normal incidence and their phase difference, respectively. It can be seen that the amplitude of the cross-polarized reflection coefficients is nearly zero, while the amplitude of the co-polarized reflection coefficients are equal to one for the working frequency band of 1.4–3.3 THz. Furthermore, the phase difference is 180° in the whole band of 1.4–3.3 THz. This proves that the LP incident wave rotates 90° and the proposed SM achieves a cross-polarization conversion of the LP wave in reflection mode.

To gain understand the physical mechanism of polarization conversion, we simulated the surface current distributions on the top and bottom layers at resonant frequencies of 1.45, 2.16, and 3.16 THz when VO_2 is in the metal phase, as shown in figure 6. Figures 6 (a) and (c) shows that there are two distinct current loops occurred on both sides of I-shape resonant at these resonant frequencies, indicating the resonance frequency of 1.45 THz and 3.16 THz is due to magnetic resonance. Meanwhile, the synthesis of surface currents is along to y -direction (figure 6 (b)). It means that the electric field of the THz incident wave couples with the I-shaped resonator, and then the electric dipole resonance forms in the y -direction. Furthermore, the surface current distributions on the top and bottom layers of an MIM metasurface structure play a crucial role in generating resonances within the



dielectric layer. At the resonant frequency of 1.45 THz, the synthesis of the top and bottom surface currents opposes but is not perfectly anti-parallel (figures 6 (a) and (d)). In contrast, at 2.16 THz, the currents are completely anti-parallel (figures 6 (b) and (e)), indicating that the resonance at 2.16 THz arises from magnetic resonance. Meanwhile, the resonance at 1.45 THz may involve a more complex interaction, combining both electric and magnetic resonances, with magnetic effects being more dominant. At a frequency of 3.16 THz, the synthesis of the top and bottom surface currents is in the same direction but not perfectly parallel (figures 6 (c) and (f)), suggesting that this resonance may also involve a complex interaction, with electric effects being more dominant. The combination of electric and magnetic resonances leads to their overlapping and coupling at various frequencies, generating multiple resonant modes [20]. This overlap enhances both the efficiency and bandwidth of polarization conversion. By leveraging the advantages of both types of resonances, a broader and more effective polarization conversion response can be achieved, as demonstrated by recent research [20, 45, 46]. Thus, the wideband RPC response observed in our SM structure is attributed to the combination of both magnetic and electric resonances.

3.3. Analysis of transmission polarization conversion

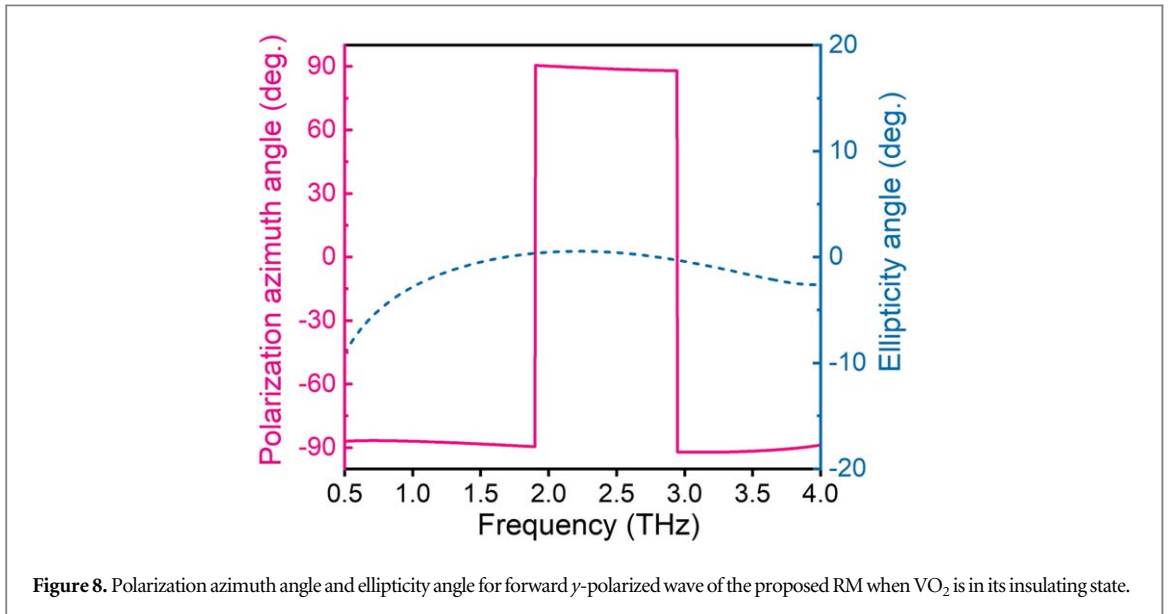
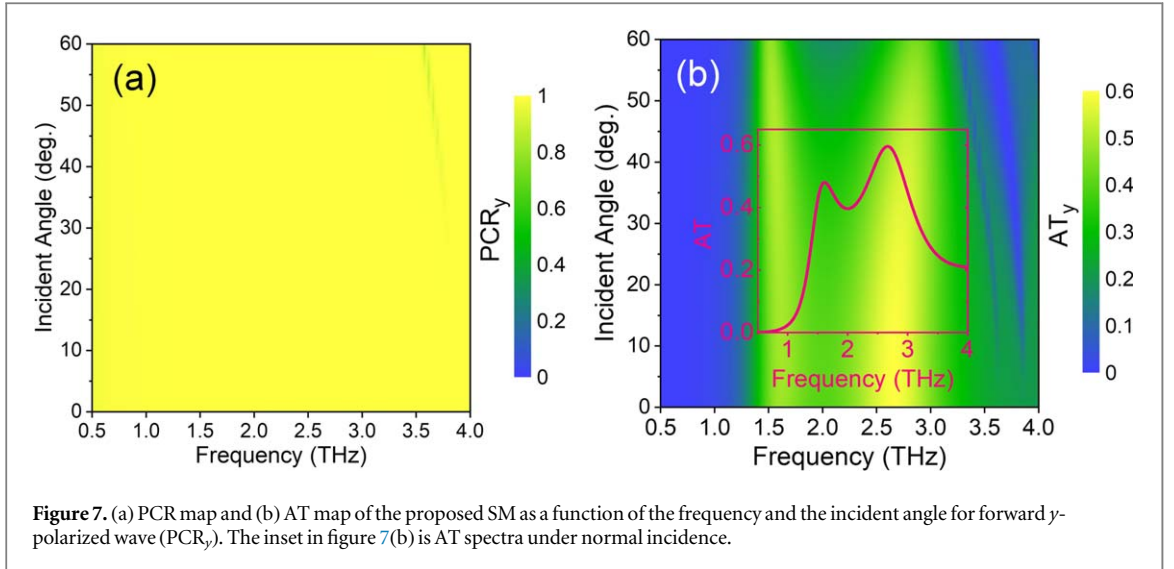
The influence of the variation of the incident angle on the PCR for forward y -polarized incident wave (PCR_y) is depicted in figure 7(a). The designed SM structure shows a stable efficiency and bandwidth with the large incident angle from 0° to 60° as seen in figure 7(a). Additionally, the asymmetric transmission (AT) parameter (Δ) for LP wave is used to determine the difference between the total transmissions in the forward and backward directions. This parameter quantifies the capability of devices for asymmetric transmission and is defined as follows [44]:

$$\Delta_{lin}^x = |t_{yx}^f|^2 - |t_{xy}^f|^2 \quad (11)$$

$$\Delta_{lin}^y = -\Delta_{lin}^x \quad (12)$$

Figure 7(b) shows the AT map of the proposed SM for forward y -polarized incident wave as a function of incident angle. Also, in the inset of figure 7(b) is AT spectrum of the designed SM at normal incidence. At normal incidence, the AT spectra shows two peaks and maximum AT parameter is 0.59. In the range of 2.38-2.92 THz, the AT value is above 0.5. However, the AT bandwidth and efficiency of the proposed metasurface reduces with increasing the incident angle. However, the AT spectra can persists its efficiency and bandwidth when the incident angle changes from 0° to 30° . These demonstrate the wide-angle insensitive PCR and AT parameter of the designed structure.

To elucidate the characteristics of the transmitted wave, Stokes parameters are employed to describe its polarization state, as detailed in [14]:



$$S_0 = t_{yy}^2 + t_{xy}^2 \quad (13)$$

$$S_1 = t_{yy}^2 - t_{xy}^2 \quad (14)$$

$$S_2 = 2t_{yy}t_{xy} \cos \delta \quad (15)$$

$$S_3 = 2t_{yy}t_{xy} \sin \delta \quad (16)$$

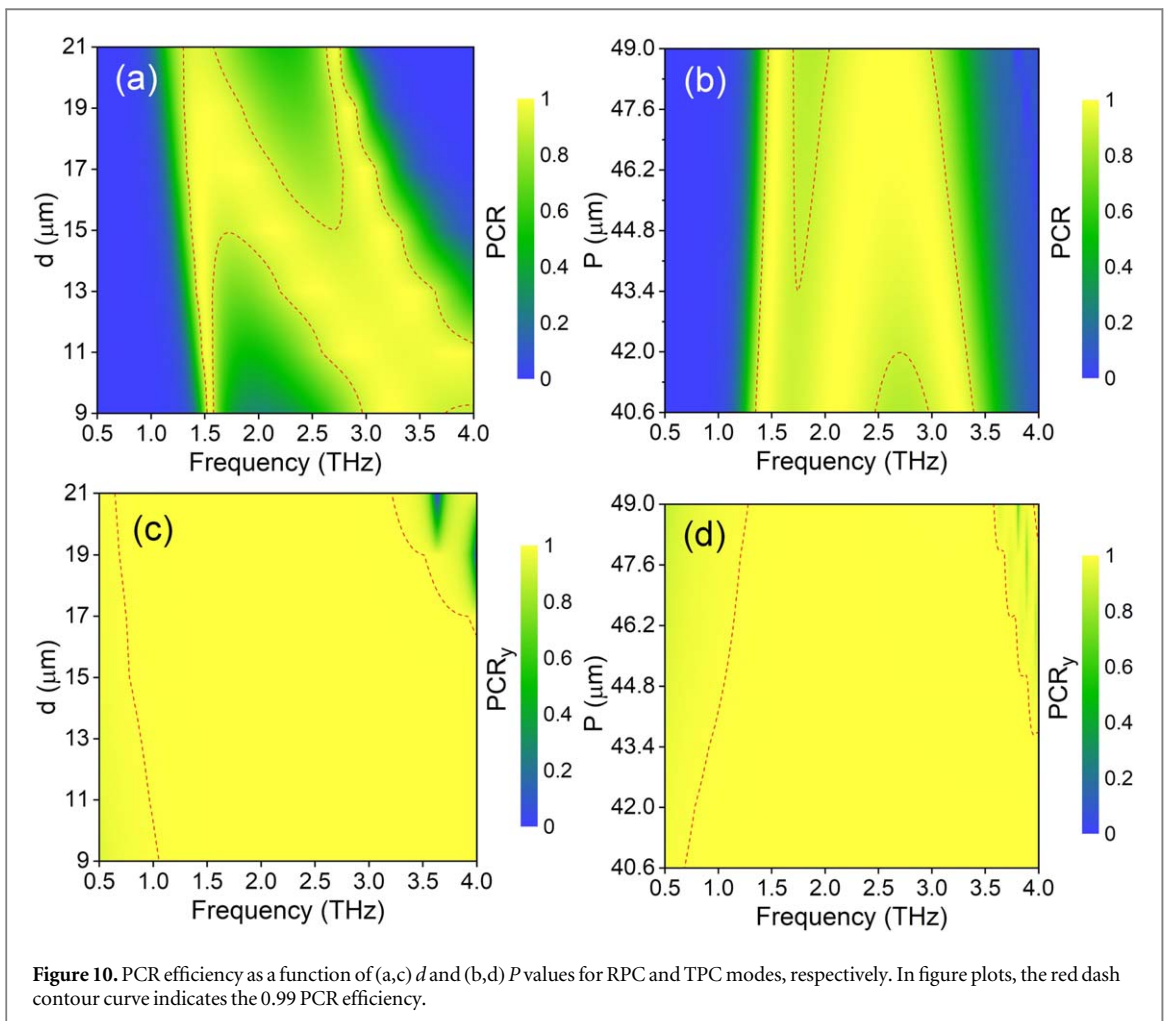
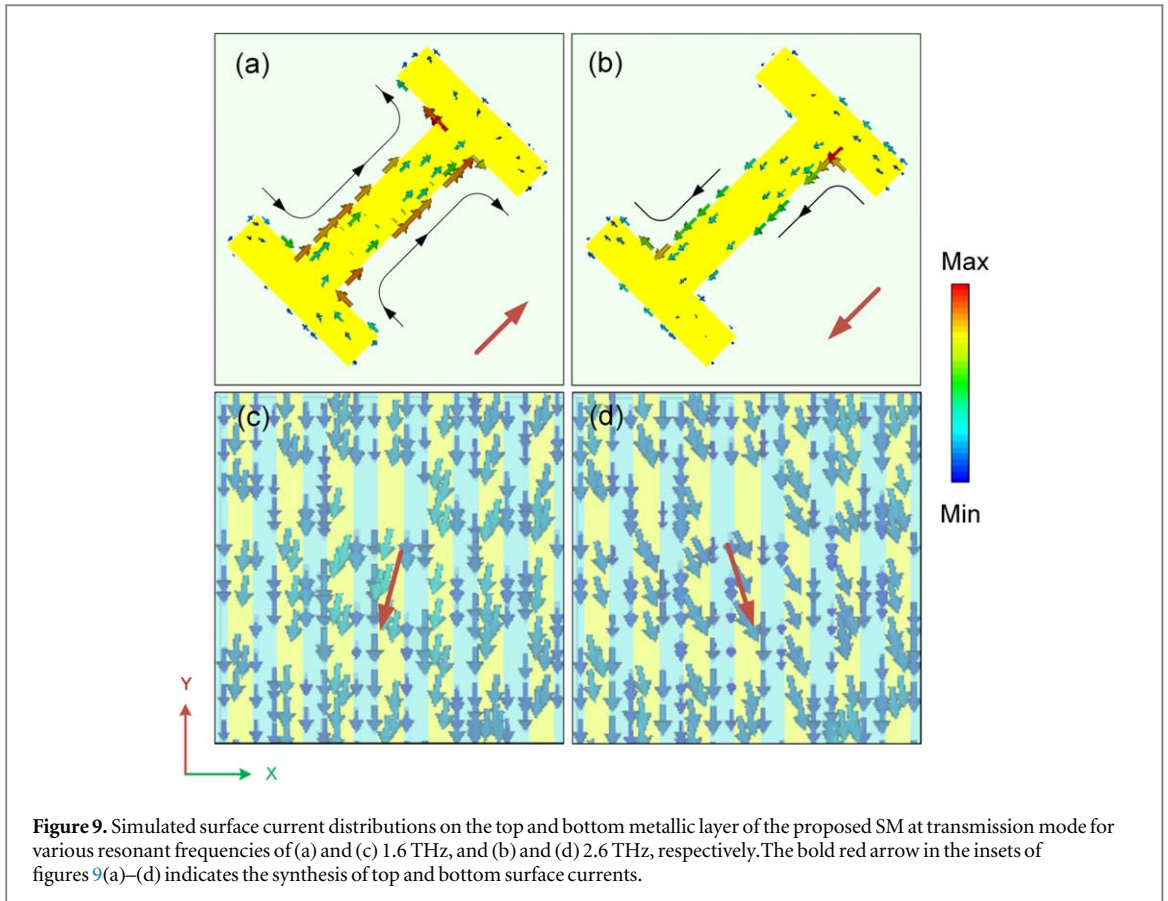
where $\delta = \arg(t_{xy}) - \arg(t_{yy})$, and the polarization azimuth angle (ψ) and ellipticity angle (η) are utilized to define the figure of merit for linear polarization conversion as follows:

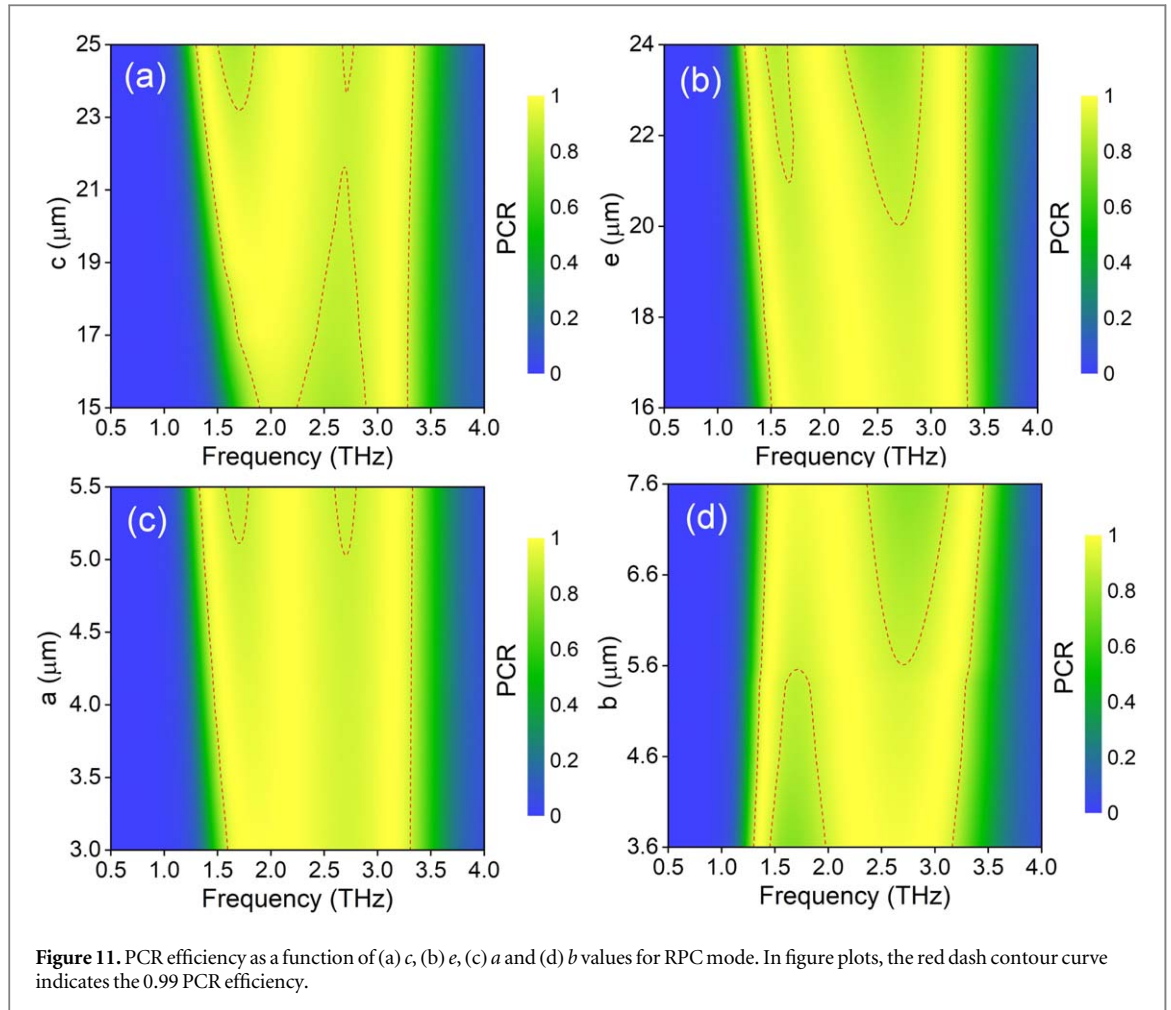
$$\psi = \frac{1}{2} \arctan\left(\frac{S_2}{S_1}\right) \quad (17)$$

$$\eta = \frac{1}{2} \arcsin\left(\frac{S_3}{S_0}\right) \quad (18)$$

Figure 8 shows the polarization azimuth angle and ellipticity angle as a function of frequency when VO₂ is in the insulator phase. As illustrated in figure 8, in the frequency range of 0.75-4.0 THz, the polarization azimuth angle is close to $\pm 90^\circ$ and the ellipticity angle is close to 0° . This observation proves that the incident y -polarized wave can be nearly perfectly converted into an x -polarized wave by the proposed SM.

To gain insight into the physical mechanism underlying coupling effects in the SM structure, whether due to magnetic resonance, electric resonance, or a combination of both, we examine the surface current distributions on the top and bottom layers of the proposed structure at the resonant frequencies of 1.6 and 2.6 THz when VO₂ is in the insulator phase. Figure 9 (a) reveals the presence of two distinct current loops, signifying that the





resonance frequency at 1.6 THz is attributed to magnetic resonance. At a higher resonant frequency of 2.6 THz, the appearance of parallel current pairs suggests the formation of electric dipoles (figure 9 (b)). Moreover, at the resonant frequency of 1.6 THz, the currents on the top and bottom surfaces oppose each other, though they are not perfectly anti-parallel (figures 9(a) and (c)). In contrast, at the higher frequency of 2.6 THz, the currents are aligned in the same direction but are not completely parallel (figures 9(b) and (d)). This observation suggests that the resonances at 1.6 THz and 2.6 THz may involve a more complex interaction that combines both electric and magnetic resonances, with magnetic effects predominating at 1.6 THz and electric effects being more pronounced at 2.6 THz. Therefore, achieving wideband polarization conversion in transmission mode is attributed to the combined effects of magnetic and electric resonances.

3.4. Influence of structural parameters on polarization conversion properties

To examine the effect of geometric parameters on the polarization conversion behavior in both RPC and TPC modes of the proposed SM structure, numerical simulations were conducted by altering one variable while keeping the others constant for a forward y -polarized incident wave. Figure 10 presents the influence of the structural parameters d and P on the PCR efficiencies for both modes. As shown in figures 10(a) and (b), the thickness (d) and period (P) have a significant influence on the operating bandwidth of the proposed SM structure in RPC mode. The widest bandwidth is achieved at $d = 15 \mu\text{m}$ and $P = 42 \mu\text{m}$. In TPC mode, as the thickness (d) and period (P) increase from $9 \mu\text{m}$ to $21 \mu\text{m}$ and $40.6 \mu\text{m}$ to $49 \mu\text{m}$, respectively, the PCR spectra exhibit a red-shift and blue-shift, as illustrated in figures 10(c) and (d). Moreover, the bandwidth decreases sharply when d exceeds $15 \mu\text{m}$ and P exceeds $42 \mu\text{m}$. Considering both RPC and TPC modes, the optimal values for d and P are $15 \mu\text{m}$ and $42 \mu\text{m}$, respectively.

Furthermore, the influence of the structural parameters c , e , a , and b on the PCR efficiency of the proposed SM in RPC mode is investigated and illustrated in figure 11. The PCR bandwidth varies significantly with changes in c , e , a , and b , as shown in figures 11(a)–(d). The widest PCR bandwidth is observed at $c = 23 \mu\text{m}$, $e = 20 \mu\text{m}$, $a = 5 \mu\text{m}$, and $b = 5.6 \mu\text{m}$. In contrast, for TPC mode, the PCR efficiency and bandwidth are relatively insensitive to changes in e and b within the ranges of $18 \mu\text{m}$ to $24 \mu\text{m}$ and $3.6 \mu\text{m}$ to $7.8 \mu\text{m}$, respectively (figures 12(b) and (d)). Meanwhile, the PCR bandwidth increases and shifts to lower

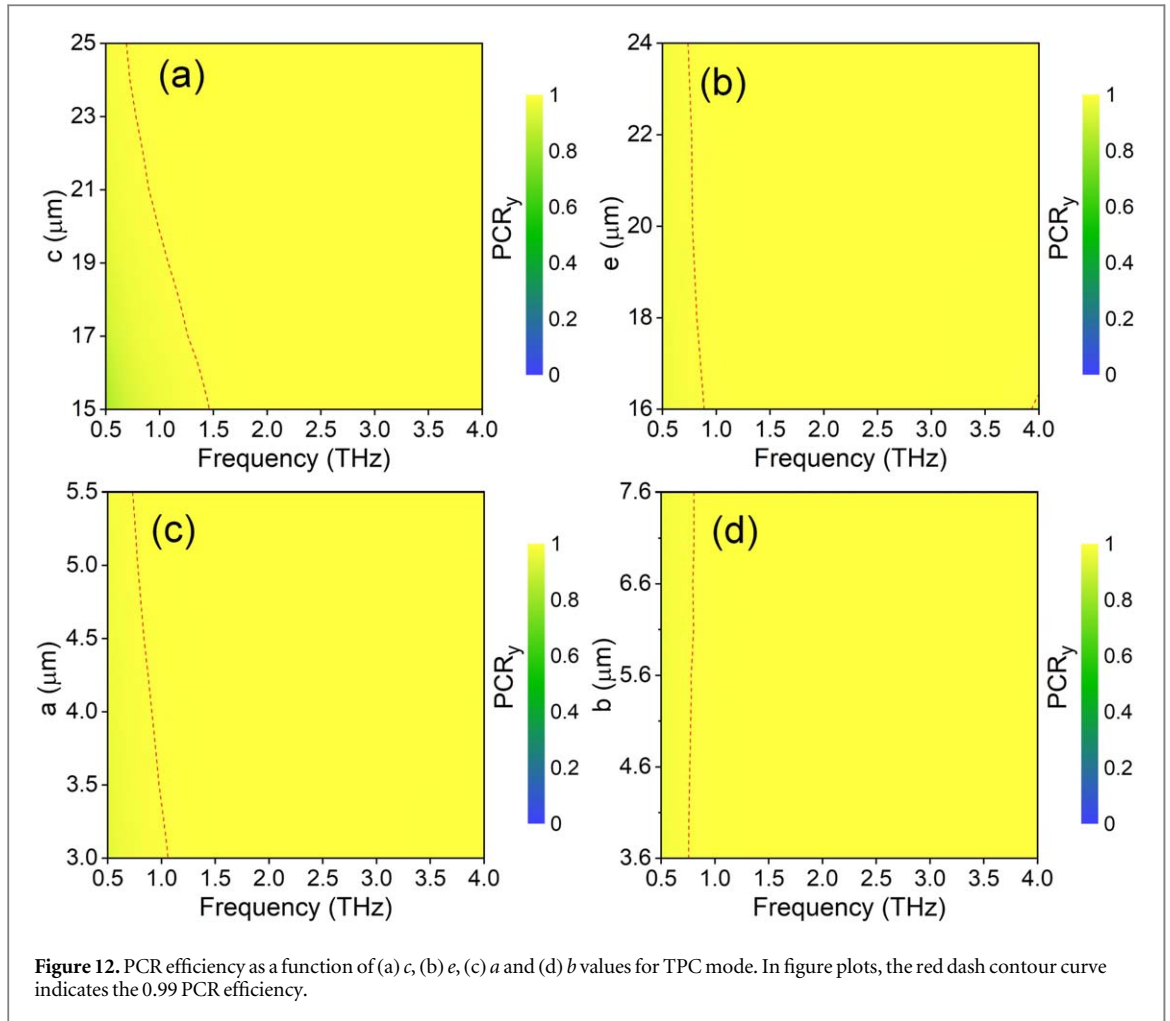


Table 1. Performance comparison of the proposed metasurface with existing works.

Reference	Function	Bandwidth (THz)	RBW (%)	Efficiency	No. layers	Tunable materials
[39]	TPC	0.5–4.75	161.9	0.99	3	VO ₂
	RPC	0.61–1.63	91.1	0.9		
[49]	TPC	0.2–1.0	133.3	0.99	2	VO ₂
	RPC	0.44–0.94	72.4	0.88		
[50]	TPC	5.3–10.7	67.5	0.9	1	VO ₂
	RPC	5.3–10.7	67.5	0.9		
[47]	TPC	1.19–3.48	98.1	0.9	1	VO ₂ , Si
	RPC	0.32–3.44	166	0.9		
This work	TPC	0.75–4.0	136.8	0.99	1	VO ₂
	RPC	1.4–3.3	80.8	0.9		

frequencies as the values of c and a increase (figures 12(a) and (c)). Therefore, to optimize polarization conversion properties for both RPC and TPC modes, the structural parameters are selected as $c = 23 \mu\text{m}$, $e = 20 \mu\text{m}$, $a = 5 \mu\text{m}$, and $b = 5.6 \mu\text{m}$.

Finally, to underscore the advanced nature of our research, we compared the functions, bandwidths, RBW, efficiency, number layers of dielectric substrate, and tunable materials from recently published works with similar functionalities in the THz region, as summarized in table 1. Our proposed structure demonstrates a simple design with the highest efficiency and moderate bandwidth for both LPC and RPC functions. Compared to the SM structures reported in [39] and [47], our design exhibits a narrower RBW. However, in comparison to the structure described in [39], our design achieves 2.53 and 3.37 times higher average bandwidth per layer for TPC and RPC modes, respectively. Meanwhile, the structure reported in [47]

requires a complex mechanism to switch between transmissive and reflective polarization conversion modes, further highlighting the effectiveness of our design. The dual functionality of the proposed metasurface, capable of switching between reflective polarization conversion (RPC) and transmissive polarization conversion (TPC) modes, greatly enhances its application potential in imaging, sensing, and communication. In sensing, RPC facilitates the detection of surface variations and material properties via reflected polarized light, while TPC allows for precise analysis of substances through transmitted polarized light. This dual-mode functionality offers a more versatile and comprehensive sensing approach for a wide range of samples and environmental conditions. Furthermore, recent advancements have demonstrated the fabrication of reflection-transmission integrated dual-mode metasurfaces for applications such as vortex beam generation and focusing [48].

4. Conclusion

We have demonstrated a wideband, high-efficiency metasurface that can switch between transmissive and reflective polarization conversion modes using the phase change material VO₂. The structure consists of an I-shaped resonator and gold-VO₂ alternating gratings sandwiched between dielectric layers. When VO₂ is in its metallic phase, the fully continuous metal layers of gold-VO₂ eliminate transmission, and the designed structure behaves as a reflective cross-polarization converter with a polarization conversion ratio exceeding 0.9 across a broad frequency range of 1.4–3.3 THz. In contrast, when VO₂ is in its insulator phase, the bottom metal gratings allow the transmission of the incoming LP THz wave, and the design behaves as a transmissive cross-polarization converter with a PCR above 0.99 in the 0.75–4.0 THz range. We have also investigated the working mechanism for both reflective and transmissive polarization conversion modes through theoretical analysis and by examining surface current distributions. The proposed metasurface offers several advantages, including facile design, high performance, and dual functionality, making it suitable for a wide range of applications such as imaging, sensing, and communication.

Data availability statement

All data that support the findings of this study are included within the article (and any supplementary files).

Author contributions

TQHN contributed to the conception of the paper. TQH Nguyen, TM Nguyen, and HQ Nguyen performed simulations and analyzed the data. TQH Nguyen wrote the paper. All the authors revised the paper.

Conflict of interest

The authors declare no competing interests.

ORCID iDs

Thi Quynh Hoa Nguyen  <https://orcid.org/0000-0002-0955-8241>

References

- [1] Rubin N A, D'Aversa G, Chevalier P, Shi Z, Chen W T and Capasso F 2019 *Science* **365** eaax1839
- [2] Nomura T, Javidi B, Murata S, Nitanai E and Numata T 2007 *Opt. Lett.* **32** 481–3
- [3] Cotrufo M, Singh S, Arora A, Majewski A and Alù A 2023 *Optica* **10** 1331–8
- [4] Zijlstra P, Chon J W M and Gu M 2009 *Nature* **459** 410–3
- [5] Li X, Lan T H, Tien C H and Gu M 2012 *Nat. Commun.* **3** 998
- [6] Wang J, Yang J Y, Fazal I M, Ahmed N, Yan Y, Huang H, Ren Y, Yue Y, Dolinar S, Tur M and Willner A E 2012 *Nat. Photonics* **6** 488–96
- [7] Deng L *et al* 2020 *Light Sci. Appl.* **9** 101
- [8] Ouyang X *et al* 2021 *Nat. Photonics* **15** 901–7
- [9] Khan M I and Tahir F A 2017 *J. Appl. Phys.* **122** 053103
- [10] Xu K K, Xiao Z Y and Tang J Y 2016 *Plasmonics* **12** 1869–74
- [11] Liu C, Bai Y, Zhou J, Zhao Q, Yang Y, Chen H and Qiao L 2019 *NPJ Comput. Mater.* **5** 93
- [12] Ako R T, Lee W S L, Atakaramians S, Bhaskaran M, Sriram S and Withayachumnankul W 2020 *APL Photonics* **5** 046101
- [13] Li J S and Bai F Q 2020 *Opt. Mater. Express* **10** 1853–61
- [14] Pan W, Chen Q, Ma Y, Wang X and Ren X 2020 *Opt. Commun.* **459** 124901

- [15] Huang X, Ma X, Gao H, Guo L and Li X 2023 *Appl. Phys. A* **129** 278
- [16] Li N, Zhao J, Tang P and Cheng Y 2024 *Opt. Commun.* **560** 130445
- [17] Xu J, Li R, Qin J, Wang S and Han T 2018 *Opt. Express* **26** 20913–9
- [18] Khan M I, Khalid Z and Tahir F A 2019 *Sci. Rep.* **9** 4552
- [19] Cao T N, Nguyen M T, Nguyen N H, Truong C L and Nguyen T Q H 2021 *Mater. Res. Express* **8** 065801
- [20] Nguyen T M, Nguyen T K T, Phan D T, Le D T, Vu D L, Nguyen T Q H and Kim J M 2022 *IEEE Access* **10** 92097–104
- [21] Nguyen T Q H, Phan H L, Nguyen T M, Nguyen N H, Le D T, Bui X K, Vu D L and Kim J M 2024 *Opt. Mater.* **154** 115682
- [22] Ding F, Zhong S and Bozhevolnyi S I 2018 *Adv. Opt. Mater.* **6** 1701204
- [23] Cai H, Chen S, Zou C, Huang Q, Liu Y, Hu X, Fu Z, Zhao Y, He H and Lu Y 2018 *Adv. Opt. Mater.* **6** 1800257
- [24] Li X, Tang S, Ding F, Zhong S, Yang Y, Jiang T and Zhou J 2019 *Sci. Rep.* **9** 5454
- [25] Sun Y, Wang Y, Ye H, Li J, Fan H, Yu L, Yu Z, Liu Y and Wu T 2022 *Opt. Commun.* **503** 127442
- [26] Li Y, Zeng L, Zhang H, Zhang D, Xia K and Zhang L 2022 *Opt. Express* **30** 34586–600
- [27] Nguyen T M, Vu D L, Nguyen T Q H and Kim J M 2022 *Sci. Rep.* **12** 18779
- [28] Qiu Y, Yan D, Feng Q, Li X, Zhang L and Li J 2023 *J. Phys. D: Appl. Phys.* **56** 415301
- [29] Jalal A, Khan M I, Qasim M and Hu B 2023 *J. Opt. Soc. Am. A* **40** 1183–90
- [30] Zhuang L, Zhang W, Chao M, Liu Q, Cheng B, Song G and Liu J 2024 *Opt. Mater. Express* **14** 483–93
- [31] Ding Z, Su W, Ye L, Zhou Y, Li W, Zou J, Tang B and Yao H 2024 *Phys. Chem. Chem. Phys.* **26** 8460–8
- [32] Phan H L, Nguyen T Q H and Kim J M 2024 *IEEE Access* **12** 11664–73
- [33] Liu G, Yang R, Zhu C and Fan Z 2024 *IEEE Photonics Technol. Lett.* **36** 1065–8
- [34] Wang D, Cai B, Yang L, Wu L, Cheng Y, Chen F, Luo H and Li X 2024 *Surfaces and Interfaces* **49** 104403
- [35] Jalal A, Khan A, Qasim M, Qureshi U U R and Moghise M 2024 *Phys. Scr.* **99** 085520
- [36] Jalal A, Qasim M and Qurashi U U R 2024 *Advanced Theory and Simulations* **7** 2400363
- [37] Huang J, Li J, Yang Y, Li J, li J, Zhang Y and Yao J 2020 *Opt. Express* **28** 7018–27
- [38] Liu M et al 2012 *Nature* **487** 345–8
- [39] Jiang Y, Zhang M, Wang W and Song Z 2022 *Phys. Scr.* **97** 015501
- [40] Wang Y, Yang R, Zhao Y and Tian J 2023 *Opt. Commun.* **530** 129196
- [41] Mao R, Wang G, Cai T, Hou H, Wang D, Wu B, Zhang W and Zhang Q 2020 *J. Phys. D: Appl. Phys.* **53** 155102
- [42] Yang H, He Y, Song Tong M, Tian Guo L, Li P and Jing Zhang Y 2024 *IEEE Trans. Antennas Propag.* **72** 5099–109
- [43] Nguyen T Q H, Phan H L, Lam V D and Kim J M 2024 *Phys. Scr.* **99** 075518
- [44] Menzel C, Rockstuhl C and Lederer F 2010 *Phys. Rev. A* **82** 053811
- [45] Zheng Q, Guo C, Yuan P, Ren Y H and Ding J 2018 *J. Electron. Mater.* **47** 2658–66
- [46] Hu J, Bandyopadhyay S, Liu Y H and Shao L Y 2021 *Frontiers in Physics* **8** 586087
- [47] Zhao R, Su L, Wang T, Cong D, Wang S and Gao Y 2024 *Diamond Relat. Mater.* **149** 111581
- [48] Faraz F, Zhang Z, Huang Y, Fraz H, Abbasi T U R, Wang X and Zhu W 2024 *Adv. Opt. Mater.* **12** 2302608
- [49] Du H, Jiang M, Zeng L, Zhang L, Xu W, Zhang X and Hu F 2022 *Chin. Phys. B* **31** 064210
- [50] Yu F Y, Wang Q C, He M X, Shen X B, Meng D S, Zhu J B and Wen Q Y 2023 *Eur. Phys. J. D* **77** 82